ISIJ International, Vol. 41 (2001), No. 12, pp. 1473–1480

Prediction and Analysis on Formation of Internal Cracks in Continuously Cast Slabs by Mathematical Models

Zhiqiang HAN, Kaike CAI[1)] and Baicheng LIU

Computer-Aided Casting Engineering Lab., Department of Mechanical Engineering, Tsinghua University, Beijing 100084, P. R. China. 1) Steelmaking Institute, Department of Metallurgy Engineering, University of Science and Technology Beijing, Beijing 100083, P. R. China.

(*Received on May 28, 2001; accepted in final form in August 21, 2001*)

The formation of internal cracks in continuously cast slabs is mainly attributed to the strain status and microsegregation near the solidifying front of the slabs. Based on this understanding, the effects of the strain status at solidifying front and the chemical composition of liquid steel on the internal cracks were studied using a strain analysis model and a microsegregation model developed in the present study. The tensile strains at the solidifying front caused by bulging, unbending, and misalignment of supporting rolls in a four-point-unbending bow caster were calculated. The roll gap in the caster was measured for the calculation of the strains caused by the misalignment of the supporting rolls. The calculated strain status near the solidifying front was used to predict the internal cracks. Critical strains based on some experimental data were adopted as the crack criteria. Sulfur prints of the slab transverse sections were used to verify the model predictions. The enrichment of chemical compositions in the interdendritic liquid and its effect on the freezing temperature of the liquid were studied with the microsegregation model, in which the transition of ferritic/austenitic solidification and the precipitation of MnS were taken into account. S and P were revealed to strongly accumulate at the columnar grain boundaries, and the segregation of P increases significantly when C content increases from 0.1 % to 0.2 %. With the accumulation of P and S in the interdendritic liquid, the freezing temperature of the liquid decreases obviously, thus the internal crack tendency is greatly increased.

KEY WORDS: continuously cast slab; internal cracks; strain analysis; microsegregation; mathematical models.

1. Introduction

Internal crack is one of the main defects in continuously cast slabs. It is very important to predict and control this defect in production of high quality and defect-free products in steel industry. It has been reported that the internal cracks are resulted from the excessive tensile strains produced at the solidifying front of the slab.[1–6)] In continuous casting process, the factors such as bulging,[7–10)] unbending or straightening,[11–13)] and misalignment of the supporting rolls[14,15)] can result in tensile strains near the solidifying front of the slab. Once the total strain applied to the solidifying front exceeds a limit strain, termed critical strain, the solidifying front will crack along the columnar grain boundaries, thus forming internal cracks in the slab. Accompanying the cracking of the solidifying front, the solute-rich liquid ahead of the solidification interface is sucked into the cracks.[1)] As a result, the internal cracks are usually accompanied by heavy segregation lines, which can be easily distinguished in sulfur prints.[16)] On the other hand, the formation of the cracks also depends on the mechanical properties of the solidifying front, especially strength and ductility, which are closely related to the microsegregation near the solidifying front.[1,17)] The enrichment of impurity elements, such as P and S, in the interdendritic liquid significantly decreases the freezing temperature of the liquid, thus obviously decreasing the deformation-resistant ability of the solidifying front. Accordingly, microsegregation is also responsible for the formation of the internal cracks.

Some researchers developed finite element models to analyze the strain status at the solidifying front as well as the strain distribution in the solidified shell of the slab, for example, the models for bulging,[7,10)] unbending,[11,12)] roll misalignment,[14,15)] and thermal strain analysis.[18)] Most of these models just focus on one or several roll pitches. However, in most cases, we do not know in which segments in the whole length of the caster will the cracks probably form. In addition, these finite element models only considered one or two factors resulting in tensile strains at the solidifying front. In continuous casting practice, people are more interested in which of the factors dominates the formation of the cracks or the combined effects of all these factors. Moreover, the huge computing time and the lack of reliable constitutive relationship describing the mechanical behavior of steel at elevated temperatures greatly restrict the application of finite element method in quick analysis and diagnosis of an under-operating continuous casting process.

In this paper, the effects of the strain status near the so-

lidifying front and the steel composition on the formation of internal cracks were studied using an empirical equation based strain analysis model and a microsegregation model developed in the present study. The tensile strains at the solidifying front caused by bulging, straightening, and misalignment of supporting rolls in a four-point-unbending bow caster were calculated. The roll gap was measured for the calculation of the strains caused by the misalignment of supporting rolls. The calculated tensile strains were used to predict the formation of the internal cracks. The sulfur prints of the slab transverse sections were used to verify the model predictions. On the other hand, the accumulation of impurity elements, mainly S and P, in the interdendritic liquid and its effect on the freezing temperature of the liquid were studied using a microsegregation model, in which the transition of ferritic/austenitic solidification and the precipitation of MnS were taken into account.

2. Mathematical Models

2.1. Strain Analysis Model

The strain analysis model for the continuously cast slab is based on a heat transfer model, which was developed to calculate the variations of surface temperature and solidified shell thickness of the slab in the casting direction. According to the characteristics of heat transfer and solidification of the slab, a quarter of the transverse section of the slab was taken as the calculation domain. The heat transfer of the domain during its movement through the mold and secondary cooling zone is described by the following two-dimensional transient heat conduction equation,

$$\rho C\frac{\partial T}{\partial t}=\frac{\partial}{\partial x}\left(\lambda\frac{\partial T}{\partial x}\right)+\frac{\partial}{\partial y}\left(\lambda\frac{\partial T}{\partial y}\right)+\rho L\frac{\partial f_s}{\partial t} \quad \text{....(1)}$$

where T is temperature, t is time, ρ, C, λ are the density, specific heat, and heat conductivity respectively. L is latent heat, and f_s is solid fraction. The model was numerically solved using the control-volume based finite difference method.[19] In the mold, the heat transfer at the slab surface was treated as a heat flux boundary. In the secondary cooling zone, the heat flux at the slab surface was calculated using heat transfer coefficients depending on the water flux on the slab surface. The main thermophysical property data used in the model are listed in **Table 1**. The solidified shell thickness is determined by using the solidus temperature after the temperature distribution in the slab is calculated.

The tensile strains at the solidifying front caused by bulging, unbending, and misalignment of supporting rolls were calculated using the following empirical equations,[15,20]

$$\varepsilon_B=\frac{1\,600S\delta_B}{l^2} \quad \text{.....(2)}$$

$$\varepsilon_S=100\times\left(\frac{d}{2}-S\right)\times\left|\frac{1}{R_{n-1}}-\frac{1}{R_n}\right| \quad \text{.....(3)}$$

$$\varepsilon_M=\frac{300S\delta_M}{l^2} \quad \text{.....(4)}$$

where ε_B, ε_S, and ε_M are the strains caused by bulging, straightening, and roll misalignment, respectively. S is solidified shell thickness, l is roll pitch, δ_B is slab bulging deflection, d is slab thickness, R_{n-1} and R_n are the unbending radii, and δ_M is the roll misalignment amount.

The slab bulging deflection δ_B was calculated using the following equation,

$$\delta_B=\frac{Pl^4}{32E_eS^3}\sqrt{t} \quad \text{.....(5)}$$

where P is the static pressure of liquid steel, t is the time for slab to travel a roll-pitch, and E_e is the equivalent elastic modulus that can be calculated using the following equation,

$$E_e=\frac{T_s-T_m}{T_s-100}\times10^6 \quad \text{N/cm}^2 \quad \text{.....(6)}$$

where T_s is solidus temperature, and T_m is the average of the surface temperature and the solidus temperature. The total strain at the solidifying front was calculated by

$$\varepsilon_T=\varepsilon_B+\varepsilon_S+\varepsilon_M \quad \text{.....(7)}$$

2.2. Microsegregation Model

The microsegregation was calculated using the equation proposed by Brody and Flemings[21] based on the assumptions of limited diffusion in solid and complete diffusion in liquid,

$$C_s^*=kC_0[1-(1-2\alpha k)f_s]^{(k-1)/(1-2\alpha k)} \quad \text{.....(8)}$$

where C_s^* is equilibrium solid concentration, C_0 is initial concentration, f_s is solid fraction, k is partition ratio, and α is a solidification parameter defined as

$$\alpha=\frac{4D_st_s}{L^2} \quad \text{.....(9)}$$

where D_s is the diffusion coefficient in solid, t_s is solidification time, and L is secondary dendrite arm spacing. The solidification time t_s is expressed by the following equation,

Table 1. The main thermophysical property data.

Properties	Values
Density (g/cm^3)	7.4
Heat capacity (Cal/g.℃)	0.16
Heat conductivity (Cal/cm. s. ℃)	0.07
Liquidus temperature (℃)	T_l=1536-{90[C%]+6.2[Si%]+1.7[Mn%]+28[P%]+40[S%]+2.6[Cu%]+2.9[Ni%]+1.8[Cr%]+5.1[Al%]}
Solidus temperature (℃)	T_s=1536-{415.3[C%]+12.3[Si%]+6.8[Mn%]+124.5[P%]+183.9[S%]+4.3[Ni%]+1.4[Cr%]+4.1[Al%]}

Table 2. Solidification parameters.[17]

Element	Ferritic			Austenitic		
	D_s (m^2s^{-1})	m (℃/%)	k	D_s (m^2s^{-1})	m (℃/%)	k
C	7.9×10^{-9}	80	0.2	6.4×10^{-10}	60	0.35
Si	3.5×10^{-11}	8	0.77	1.1×10^{-12}	8	0.52
Mn	4.0×10^{-11}	5	0.75	4.2×10^{-13}	5	0.75
P	4.4×10^{-11}	34	0.13	2.5×10^{-12}	34	0.06
S	1.6×10^{-10}	40	0.06	3.9×10^{-11}	40	0.025

$$t_s = \frac{T_l - T_s}{\partial T/\partial t} \quad \text{.....(10)}$$

where T_l is liquidus temperature, and T_s is solidus temperature. The secondary dendrite arm spacing can be expressed as the function of cooling rate,[22]

$$L = 146\times10^{-6}\left(\frac{\partial T}{\partial t}\right)^{-0.39} \quad \text{.....(11)}$$

For $\alpha=0$ (corresponding to no diffusion in solid) Eq. (8) reduces to the Scheil equation.[23] However, for complete diffusion ($\alpha\to\infty$) no microsegregation appears, conflicting with equilibrium solidification. To improve the model for high α-values, the equation proposed by Clyne and Kurz[24] was used to correct α,

$$\alpha' = \alpha(1-e^{-1/\alpha}) - \frac{1}{2}e^{-1/2\alpha} \quad \text{.....(12)}$$

For high α-values α' approaches 0.5, which substituted in Eq. (8) leads to equilibrium model. For low α-values α' equals α, the model is not alternated. There is no physical justification for this correction, it is purely mathematical and was chosen to give the correct results at the two extremes of high and low α.

The mutual effects between alloy components on microsegregation were assumed negligible except for the extreme of containing very high content of alloy elements. For each component, microsegregation was calculated by using Eq. (8), and the liquidus temperature as well as the temperatures corresponding to any solid fractions was calculated by summing the contributions of all alloy elements,

$$T_l = T_p - \sum_i m_i C_{0,i} \quad \text{.....(13)}$$

$$T = T_p - \sum_i (m_i/k_i) C^*_{s,i} \quad \text{.....(14)}$$

where the subscript i denotes different alloying components. T_p is fusion temperature of pure iron.

In solidification of steel, two solid phases can be distinguished, one is the ferritic (δ) crystal structure (bcc) and the other one is the austenitic (γ) crystal structure (fcc). For steel with carbon content lower than 0.1%, only ferritic crystal structure develops in the whole solidification. For steel with carbon content over 0.5%, only austenitic crystal structure develops in the whole solidification process. While for steel with carbon content lower than 0.5% and higher than 0.1%, the liquid steel firstly solidifies as ferritic phase, but when the carbon concentration in the interdendritic fluid exceeds 0.5%, the residual liquid will solidify as austenitic crystal structure. This transition of solidification mode has important influences on the microsegregation because of the very different solidification parameters in the two crystal phases (see **Table 2**).

To incorporate this effect in the model it is assumed that only carbon concentration controls this transition and other components do not influence the transition. Using Eq. (8) the solid fraction at which the transition occurs can be calculated,[17]

$$f_{s,\delta\to\gamma} = \frac{1}{1-2\alpha k}\left[1-\left(\frac{0.5}{C_0}\right)^{(1-2\alpha k)/(k-1)}\right] \quad \text{.....(15)}$$

where the ferritic data should be employed for α and k. In order to calculate the microsegregation at any solid fraction higher than $f_{s,\delta\to\gamma}$, a virtual zero concentration must be calculated. Based on Eq. (8) and the solidification parameters in austenitic phase, the virtual zero concentration would lead to the same concentration in residual liquid at the transition point. The virtual zero concentration can be calculated by the following equation,[17]

$$C'_0 = C_{l,\delta\to\gamma}[1-(1-2\alpha k)f_{s,\delta\to\gamma}]^{(1-k)/(1-2\alpha k)} \quad \text{.....(16)}$$

where the austenitic data should be employed for α and k.

Sulfur is a strongly segregating element (low partition ratio), but its influence is limited by the precipitation of MnS. The solubility of MnS is $0.506(\%)^2$ at 1 500°C.[17] If the product of Mn and S concentrations exceeds this value, MnS will precipitate. With the precipitation of MnS, the S concentration decreases significantly without considerable change of the Mn concentration because the later is far higher than the S concentration. So, in present study, the S concentration in the interdendritic liquid was adjusted to satisfy the solubility demand and the Mn concentration was maintained unchanged once the product of these two concentrations exceeded the solubility.

In the solution of this model, the cooling rate should be determined in prior. According to Cornelissen,[17] the cooling rates during solidification are in the range of 186.5–0.19°C/s from the surface to the center of a 210 mm thick slab, and the corresponding dendrite arm spacing varies from 19 to 280 μm. Considering that the internal cracks usually occur in the fully developed columnar grain zones in the slab, the dendrite arm spacing in these zones was measured. Based on the measured results, the dendrite arm spacing in the present model is taken as 200 μm, its corresponding cooling rate is 0.45°C/s. An iterative procedure is employed for solving the model. Firstly, the solidus temperature is artificially assumed. By using the assumed temperature, C^*_s can be calculated, based on which the solidus temperature can be updated. The iteration is terminated when the solidus temperature becomes convergent. After

the solidus temperature is determined, the concentrations and freezing temperatures of the interdendritic liquid corresponding to any solid fractions can be calculated by using Eqs. (8) and (14).

3. Results and Discussion

The calculation was based on a fully bowed continuous caster that has 18 segments and 98 pairs of rolls in its secondary cooling zone. The roll diameter and the roll pitch vary from ϕ155 mm to ϕ325 mm and from 199 mm to 370 mm, respectively. The metallurgical length of the caster is about 33 m. The radius of the caster is 10.5 m. A four-point unbending system is equipped in the caster, in which the unbending radii are 13.5, 19.5, and 38.0 m.

3.1. Validity of Heat Transfer Model

The reliability of the heat transfer model is very important to the validity of the strain analysis model. The results of the heat transfer model were verified by using measured surface temperature and liquid core length data provided by the caster manufacturer. Four positions were selected as measurement points along the length of the slab, and the mid-width surface temperatures at these points were measured with a color comparator pyrometer. **Figure 1** shows the comparison of the measured and the calculated surface temperatures. Although the calculated temperature has some deviation at the second measurement point, the overall prediction shows good agreement with the measured results. In addition, the data of liquid core length provided by the caster manufacturer were used for further verification of the heat transfer model. The calculated results of the liquid core length under various process conditions were listed in **Table 3**. It is shown that the relative error of the predicted results is usually less than 5%, and the maximum error is no more than 8%. It is proved that the heat transfer model has the ability to provide reliable data for the strain analysis model.

3.2. Strain Distribution Characteristics

The calculated bulging strain and straightening strain at the solidifying front along the length of the slab are shown in **Fig. 2**. It can be seen that considerable bulging strain occurs immediately when the slab moves out of the mold, however, the strain decreases soon. After that, the bulging strain gradually increases and then decreases again. A large variety of calculations showed that although the magnitude of the bulging strain varies when the process condition is changed, the distribution of the strain along the length of the slab nearly has the same characteristics. The slab bulging between two adjacent rolls mainly depends on the static pressure of liquid steel, the roll pitch, and the stiffness of the solidified shell. When the slab just moves out of the mold, although the static pressure and the roll pitch are relatively small, severe bulging occurs because of the thin solidified shell and high surface temperature, correspondingly, the bulging strain at the solidifying front is very large. However, the bulging decreases very quickly due to the intensive cooling from the spraying water. With further downward movement of the slab, the static pressure of the liquid steel increases significantly and the roll pitch also increases to some extent, while the thickness of the solidified shell has not increased to a certain level at which the shell is strong enough to resist the static pressure, thus consider-

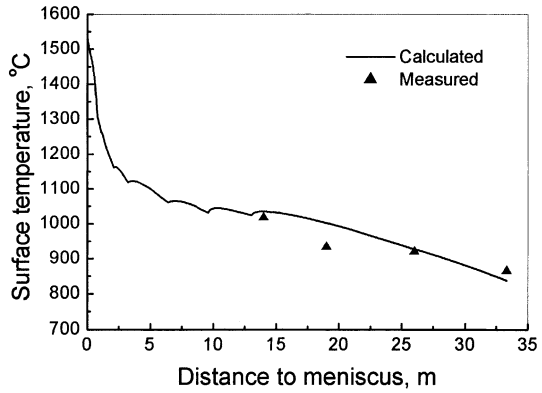

Fig. 1. The comparison of calculated and measured surface temperatures; steel composition C 0.16, Si 0.30, Mn 1.44, P 0.012, S 0.008%; section size 1 300×250 mm; tundish temperature 1 526–1 529°C; casting speed 1.0–1.1 m/min.

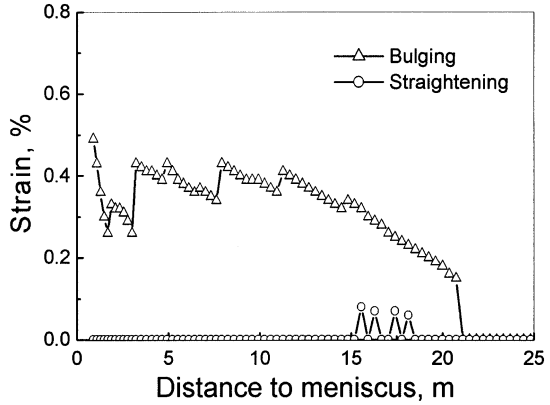

Fig. 2. The distribution of bulging and straightening strains along the slab length; carbon steel; section size 1 550×230 mm; tundish temperature 1 535°C; casting speed 1.0 m/min.

Table 3. The calculated and caster manufacturer provided liquid core length data.

Steel	Section size (mm)	Casting speed (m/min)	Cooling water (L/Kg steel)	Liquid Core Length		
				Caster manufacturer provided (m)	Predicted (m)	Relative error (%)
Carbon steel	1550x230	1.2	0.84	23.0	24.8	+7.8
	1550x250	1.2		28.2	28.8	+2.1
Structural steel	1550x210	1.2	0.76	20.5	21.4	+4.4
	1550x230	1.0		20.0	20.7	+3.5
	1550x250	1.0		24.5	24.0	-2.1
Low alloy steel	1550x210	1.0	0.52	17.5	17.9	+2.3
	1550x230	1.0		20.8	20.7	-0.5

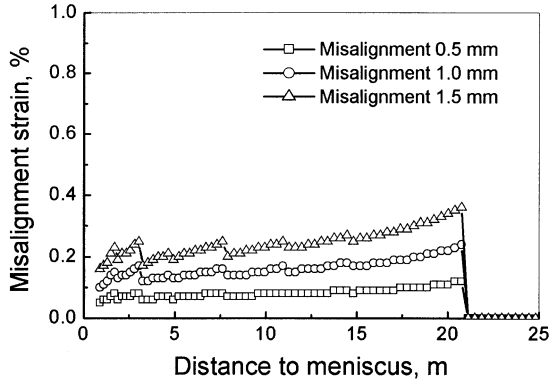

Fig. 3. The distribution of roll misalignment strains along the slab length; carbon steel; section size 1 550×230 mm; tundish temperature 1 535°C; casting speed 1.0 m/min.

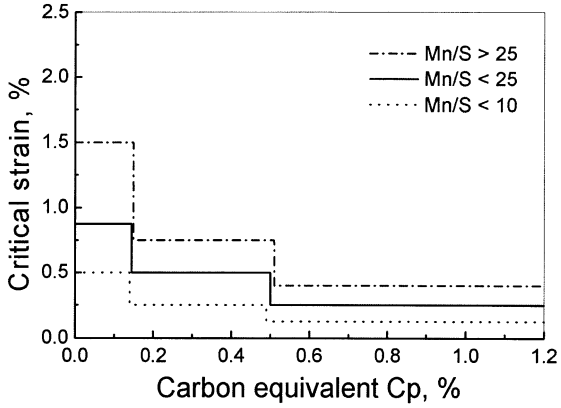

Fig. 4. The relationship between critical strain and steel composition.[25] Cp=C+0.02Mn+0.04Ni−0.1Si−0.04Cr−0.1Mo

able bulging takes place again. As a result, very serious tensile strain occurs at the solidifying front. In the segments near the end of the liquid core, the slab bulging decreases again because the solidified shell is enough thick to hold the static pressure. The straightening strain originates in the unbending zone of the caster and occurs as tensile strain at the solidifying front of the upper solidified shell of the slab. In general, the straightening strain is about 0.1% and is only 15–20% of the bulging strain for a multi-point unbending caster, which is shown in Fig. 2.

The misalignment of supporting rolls can cause additional strain at the solidifying front of the slab. **Figure 3** shows the strains caused by assumed amounts of roll misalignment, 0.5, 1.0, and 1.5 mm. It is necessarily to state that this figure does not represent a real distribution of the misalignment strain. Each datum point in the figure only represents the strain caused by the corresponding roll that is assumed to be the only misaligned one in the whole caster. It shows that the strain caused by a given amount of misalignment in the segments with a thicker solidified shell is higher than that in the segments with a thinner solidified shell. In other words, the harmful effect of the roll misalignment is especially significant in segments where the solidified shell is relatively thick. So, more attention should be paid to the position precision of the rolls located in the middle and lower parts of the caster.

3.3. Effect of Strain Status on Internal Cracks

The calculated strains near the solidifying front were used to predict the internal cracks in the slab. In the prediction, critical strains were adopted as the crack criteria. For a considered process condition, if the total strain at the solidifying front exceeds the critical strain, internal cracks are predicted to form. Otherwise, the slab is predicted to be free from the cracks. The critical strains mainly depend upon the steel composition and the strain rate at the solidifying front.[1,4,6,25] With the increase of carbon content and the decrease of the content ratio of Mn to S, the critical strain decreases, and with the decreasing of the strain rate at solidifying front, the critical strain increases. In this study, the critical strains were chosen from the results provided by Hiebler *et al.*[25] who summarized the experimental data from many researchers and gave the relationship between the critical strains and the steel compositions, which is shown in **Fig. 4**.

The strain analysis model was verified by comparing the model predictions with the sulfur prints of practically produced slabs. Two examples were introduced to illustrate the model predictions. **Figure 5** shows the sulfur prints of the transverse sections of the two slabs. The process parameters of the slabs are listed in **Table 4**. In order to calculate the strain caused by the misalignment of supporting rolls, the roll gap of the caster was measured using a multi-functional roll gap measurement instrument. **Figure 6** shows the measured roll gap data along the length of the caster (corresponding to sulfur print No. 1882). In the calculation, the misalignment amount of each roll, δ_M, is taken as the difference of the measured and target roll gap data. By using the process parameters of the two slabs, whether the internal cracks form and how the cracks extend in the slabs were predicted. The predicted results for the slab corresponding to the sulfur print No. 1882 were shown in **Fig. 7**. From the figure it can be seen that in the range of 1.5–18 m to the meniscus, the total tensile strain at the solidifying front exceeds the critical strain, 0.5%, thus it was predicted that internal cracks would be formed. By referring the variation of the solidified shell thickness along the length of the slab, it was predicted that the internal cracks most likely to appear on the transverse section in the scope of 13–72 mm under the wide surface of the slab. The sulfur print showed that the cracks mainly located in the scope of 20–80 mm under the surface of the slab. This prediction basically coincides with the real situation of the internal cracks in the slab. On the other hand, the process condition of the slab corresponding to sulfur print No. 1939 was also calculated using the strain analysis model. The calculated results (see **Fig. 8**) show that the total tensile strain at solidifying front is lower than the critical strain in the whole length of the caster, thus the slab was predicted to be free from the cracks. This prediction was well supported by the sulfur print of the slab (see Fig. 5(b)).

Actually, the main difference between the two process conditions is the content of P and S in the steel. With the increasing of S content (*i.e.* decreasing of the content ratio of Mn to S), the critical strain is decreased (see Fig. 4), and the crack susceptibility of the steel is increased. The effect of S content on the internal crack tendency is also supported by the statistic data from the sulfur prints of 200 slabs,

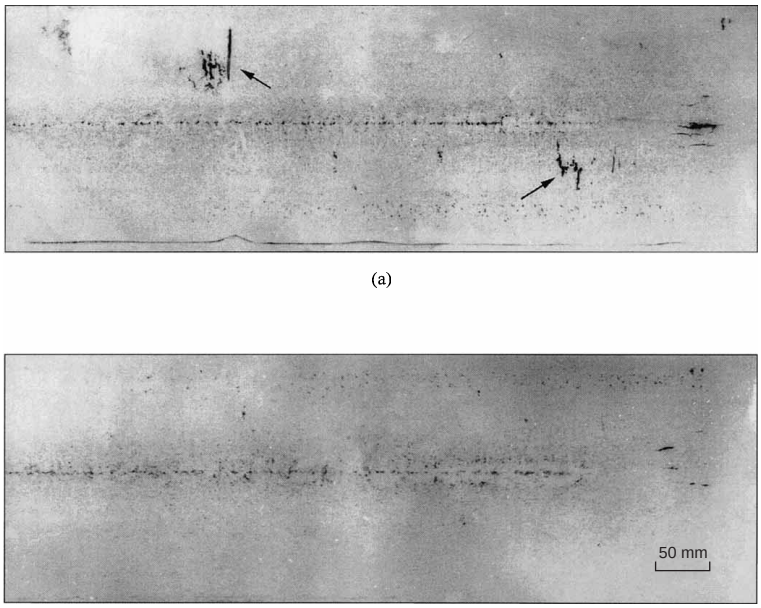

(a)

(b)

Fig. 5. The sulfur prints of the slab transverse sections; (a) with (No. 1882) and (b) without (No. 1939) internal cracks.

Table 4. The process parameters of the slabs.

Item	Sulfur print No. 1882	Sulfur print No. 1939
Steel composition (wt%)	C 0.165, Si 0.25, Mn 0.484, P 0.024, S 0.022, Al 0.018	C 0.168, Si 0.24, Mn 0.435, P 0.014, S 0.014, Al 0.015
Carbon equivalent C_p (wt%)	0.1497	0.1527
Content ratio of Mn to S	22.0	31.1
Critical strain (%)	0.50	0.75
Section size (mm)	230×1550	230×1550
Casting speed (m/min)	1.2	1.2
Tundish temperature (℃)	1539	1536

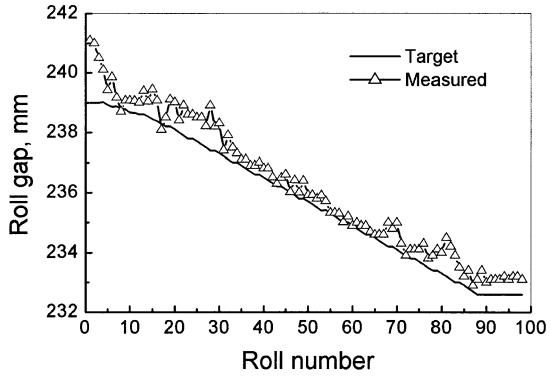

Fig. 6. The measured roll gap data (corresponding to sulfur print No. 1882).

which is shown in **Fig. 9**. In the figure, the internal crack probability is defined as the percentage of the slabs with internal cracks in the total slabs containing nearly the same S content. Although it shows some randomicity, the crack probability increases obviously with the increase of S content. When the S content exceeds 0.015%, the crack probability is higher than 80%. Besides the crack probability, the severity of the cracks is also closely related to the S content. The statistic data show that no internal cracks form when the S content is less than 0.005%, severe cracks form when the S content is higher than 0.015%, and slight cracks form when the S content is in the range of 0.005–0.015%.

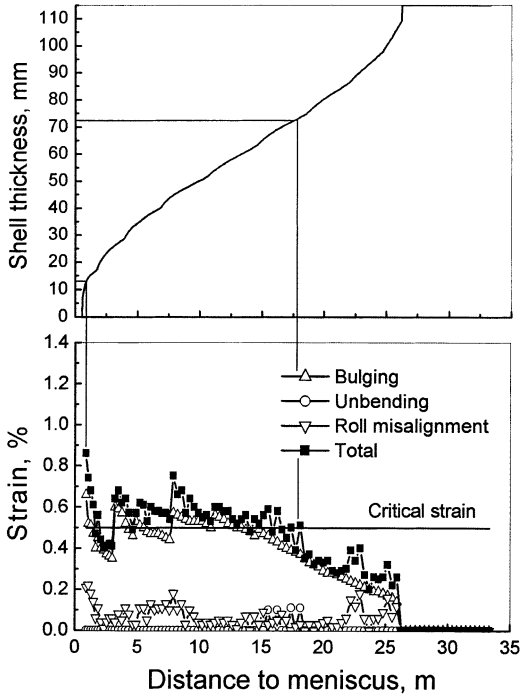

Fig. 7. The model prediction for the slab corresponding to sulfur print No. 1882.

3.4. Interdendritic Segregation in Solidification Process

The concentration and freezing temperature of the interdendritic liquid during solidification were calculated using

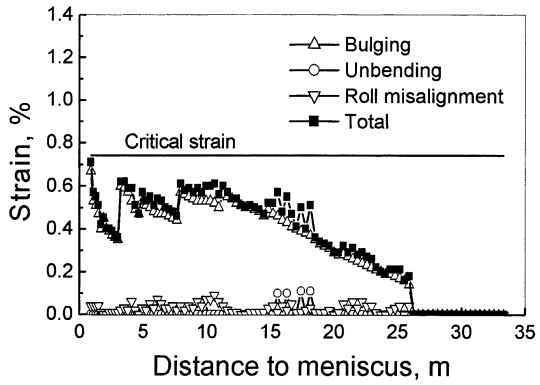

Fig. 8. The model prediction for the slab corresponding to sulfur print No. 1939.

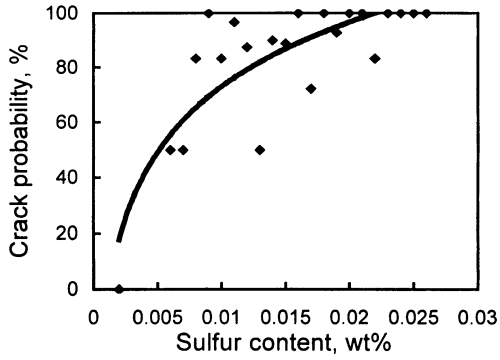

Fig. 9. The effect of sulfur content on the internal crack probability; steel composition C 0.14–0.20, Si 0.17–0.24, Mn 0.30–0.45, and P<0.025%.

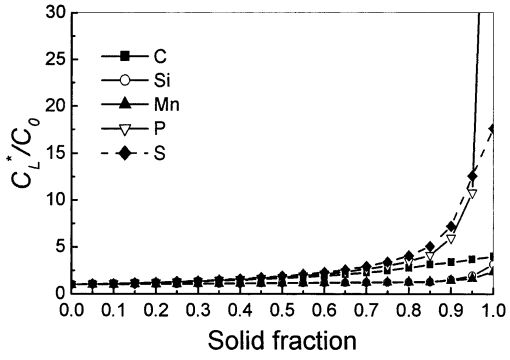

(a)

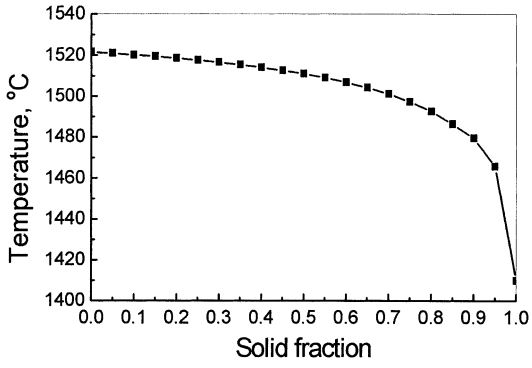

(b)

Fig. 10. The calculated (a) segregation and (b) freezing temperature of the interdendritic liquid; steel composition C 0.16, Si 0.21, Mn 0.4, P 0.02, S 0.03%.

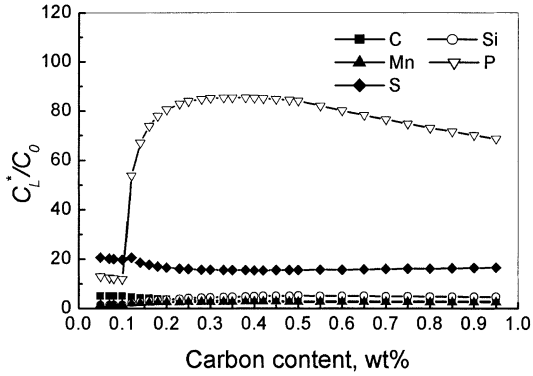

Fig. 11. The effect of carbon content on the interdendritic segregation; steel composition Si 0.21, Mn 0.4, P 0.02, S 0.03%.

the microsegregation model. The calculated results were shown in **Fig. 10**. In the figure, the vertical axis denotes the ratio of the interdendritic liquid concentration to the initial liquid concentration. It can be seen that with the increase of the solid fraction, the concentration in the interdendritic fluid increased gradually. When the solid fraction exceeds 0.9, the segregation of S and P increases significantly while that of C, Si, and Mn has no considerable change and keeps at a relatively low level. With the increasing of P and S segregation, the freezing temperature of the interdendritic liquid decreases especially when the solid fraction is higher than 0.9.

3.5. Effect of Carbon Content on Segregation and Freezing Temperature of Interdendritic Liquid

The effect of C content on the interdendritic segregation was also calculated using the microsegregation model. The calculated results are shown in **Fig. 11**, in which the vertical axis represents the ratio of the interdendritic liquid concentration at the end of solidification to the initial concentration of the steel. The segregation of C, Si, and Mn is quite light and nearly does not change with the variation of C content of the steel, while the segregation of S and P is quite heavy. It should be particularly noted that the segregation of P increases suddenly as the C content increases from 0.1% to 0.2%. It can be seen in Table 2 that the diffusion coefficients of C are two-order of magnitude higher than those of other elements whatever in ferrite or in austenite, and the partition ratios of C are far higher than those of S and P. It means that carbon does not strongly segregate during solidification. This is supported by the model calculation. However, it is well known that carbon content does have significant influence on the formation of the internal cracks. Actually, the effect of C content on the formation of internal cracks is not caused by the segregation of carbon itself. With the increase of C content, the solidification mode of the steel is changed from ferritic to ferritic–austenitic. Compared with the solidification parameters in ferritic phase, the partition ratios of S and P in austenitic phase reduce by more than one half and the diffusion coefficients also decrease by one order of magnitude (see Table 2). Therefore, with the occurrence of the austenitic phase in

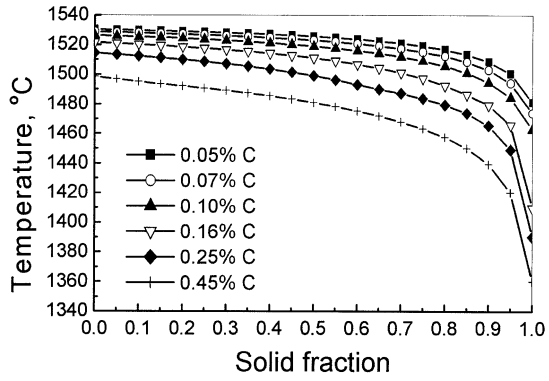

Fig. 12. The effect of carbon content on the freezing temperature of interdendritic liquid; steel composition Si 0.21, Mn 0.4, P 0.02, S 0.03%.

solidification, the segregation of P increases significantly. The segregation of S has no considerable change with the variation of the C content. This is a reflection of the suppression of Mn to S in the residual liquid. However, the accumulation of sulfur in the interdendritic liquid is still considerable.

Figure 12 shows the effect of C content on the freezing temperature of the interdendritic liquid. For a steel containing C less than 0.1%, the freezing temperature of the interdendritic liquid at the end of solidification does not decrease considerably. While for a steel containing C more than 0.1%, the freezing temperature of the interdendritic liquid decreases significantly at the end of solidification. The lower the freezing temperature, the larger the brittle region in the slab, and the higher the formation tendency of internal cracks. The effect of the C content on the formation of the internal cracks is also illustrated by statistic data. In contrast to the steel containing C 0.14–0.18% (its statistic data are shown in Fig. 9), internal cracks rarely occur in the steel containing C 0.07%. The statistic data of randomly selected 46 slabs showed that only 3 of them contain internal cracks. The process conditions and chemical compositions of these two steels are nearly the same except for the difference in C content. These statistic data from continuous casting practice justify the microsegregation model, and at the same time, the theoretical model reveals the inherent reasons for the effect of the C content on the formation of the internal cracks.

4. Conclusions

The formation of internal cracks in continuously cast slabs was studied using a strain analysis model and a microsegregation model. The study leads to the following conclusions:

A strain analysis model for calculating the tensile strains at the solidifying front caused by bulging, straightening, and misalignment of supporting rolls was developed. By using the model, the total strain at the solidifying front of the slabs produced with a four-point unbending bow caster was calculated. The internal cracks were predicted by comparing the strain status at the solidifying front with experimental data based critical strains. The sulfur prints of the slabs showed that the predicted results basically coincide with the real situations of the internal cracks.

A microsegregation model for the solidification of continuously cast slabs was developed, in which the transition of ferritic/austenitic solidification and the precipitation of MnS were considered. The model revealed that the accumulations of S and P in the interdendritic liquid are the primary causes resulting in the decrease of the freezing temperature of the liquid. The carbon content in steel has significant influence on the interdendritic segregation of P. The steel containing carbon more than 0.1% shows strong tendency to internal cracks because of the occurrence of austenitic phase in solidification process.

REFERENCES

1) A. Yamanaka, K. Nakajima and K. Okamura: *Ironmaking Steelmaking*, **22** (1995), 508.
2) K. Kim, H. N. Han, T. Yeo, Y. Lee, K. H. Oh and D. N. Lee: *Ironmaking Steelmaking*, **24** (1997), 249.
3) S. Nagata, T. Matsumiya, K. Ozawa and T. Ohashi: *Tetsu-to-Hagané*, **76** (1990), 214.
4) T. Matsumiya, M. Ito, H. Kajioka, S. Yamaguchi and Y. Nakamura: *Trans. Iron Steel Inst. Jpn*., **26** (1986), 540.
5) K. Wunnenberg and R. Flender: *Ironmaking Steelmaking*, **12** (1985), 22.
6) J. Miyazaki, K. Narita, T. Nozaki and T. Mori: *Trans. Iron Steel Inst. Jpn*., **21** (1981), B210.
7) K. Okamura and H. Kawashima: *ISIJ Int*., **29** (1989), 666.
8) A. Yoshii and S. Kihara: *Trans. Iron Steel Inst. Jpn*., **26** (1986), 891.
9) K. Miyazawa and K. Schwerdtfeger: *Ironmaking Steelmaking*, **6** (1979), 68.
10) A. Grill and K. Schwerdtfeger: *Ironmaking Steelmaking*, **6** (1979), 131.
11) M. Deisinger and K. H. Tacke: *Ironmaking Steelmaking*, **24** (1997), 321.
12) M. Uehara, I. V. Samarasekera and J. K. Brimacombe: *Ironmaking Steelmaking*, **13** (1986), 138.
13) K. H. Tacke: *Ironmaking Steelmaking*, **12** (1985), 87.
14) B. Barber, B. M. Leckenby and B. A. Lewis: *Ironmaking Steelmaking*, **18** (1991), 431.
15) B. Barber and A. Perkins: *Ironmaking Steelmaking*, **16** (1989), 406.
16) H. Fujii, T. Ohashi and T. Hiromoto: *Trans. Iron Steel Inst. Jpn.*, **18** (1978), 510.
17) M. C. M. Cornelissen: *Ironmaking Steelmaking*, **13** (1986), 204.
18) A. Grill, J. K. Brimacombe and F. Weinberg: *Ironmaking Steelmaking*, **3** (1976), 38.
19) S. V. Patankar: Numerical Heat Transfer and Fluid Flow, Hemisphere, New York, (1980).
20) Y. P. Sheng, J. Q. Sun and M. Zhang: *Iron Steel*, **28** (1993), 20.
21) H. D. Brody and M. C. Flemings: *Trans. AIME*, **236** (1966), 615.
22) M. M. Wolf and W. Kurz: *Metall. Trans*., **12B** (1981), 85.
23) M. C. Flemings: Solidification Processing, McGraw-Hill, New York, (1974), 31.
24) T. W. Clyne, M. M. Wolf and W. Kurz: *Metall. Trans*., **13B** (1982), 259.
25) H. Hiebler, J. Zirngast, C. Bernhard and M. M. Wolf: Steelmaking Conf. Proc., ed. by T. A. Danjczek, ISS, Warrendale, PA, (1994), 405.